Niobium oxyphosphate nanosheet assembled two-dimensional anode material for enhanced lithium storage

Bo Wen [a,1], Ruiting Guo [a,1], Xiong Liu [a], Wen Luo [a], Qiu He [b], Chaojiang Niu [a], Jiashen Meng [a], Qi Li [a,*], Yan Zhao [b], Liqiang Mai [a,c]

[a] State Key Laboratory of Advanced Technology for Materials Synthesis and Processing, Wuhan University of Technology, Wuhan 430070, Hubei, China
[b] State Key Laboratory of Silicate Materials for Architectures, Wuhan University of Technology, Wuhan 430070, Hubei, China
[c] Foshan Xianhu Laboratory of the Advanced Energy Science and Technology Guangdong Laboratory, Foshan 528216, Guangdong, China

ARTICLE INFO

ABSTRACT

The development of high-capacity and high-rate anodes has become an attractive endeavor for achieving high energy and power densities in lithium-ion batteries (LIBs). Herein, a new-type anode material of reduced graphene oxide (rGO) supported niobium oxyphosphate ($NbOPO_4$) nanosheet assembled two-dimensional composite material ($NbOPO_4$/rGO) is firstly fabricated and presented as a promising high-performance LIB anode material. In-depth electrochemical analyses and in/ex situ characterizations reveal that the intercalation-conversion reaction takes place during the first discharge process, followed by the reversible redox process between amorphous $NbPO_4$ and Nb which contributes to the reversible capacity in the subsequent cycles. Meanwhile, the lithiation-generated Li_3PO_4, behaving as a good lithium ion conductor, facilitates ion transport. The rGO support further regulates the structural and electron/ion transfer properties of $NbOPO_4$/rGO composite compared to neat $NbOPO_4$, resulting in greatly enhanced electrochemical performances. As a result, $NbOPO_4$/rGO as a new-type LIB anode material achieves a high capacity of 502.5 mAh g^{-1} after 800 cycles and outstanding rate capability of 308.4 mAh g^{-1} at 8 A g^{-1}. This work paves the way for the deep understanding and exploration of phosphate-based high-efficiency anode materials for LIBs.

1. Introduction

Nowadays, lithium-ion batteries (LIBs) with higher energy and power densities are required to meet the demands of their emerging applications in hybrid electrical vehicles [1–4]. However, the low theoretical capacity (372 mAh g^{-1}) of the commercial graphite anode impedes its long-term application in higher energy density devices [5,6]. Therefore, development of high-performance anode materials to meet the increasing market demand is highly desired [7]. In the past few years, great progresses have been achieved in the investigation of metal oxides [8–10] and metal/alloy materials [11,12] as anodes for LIBs. These anode materials generally suffer from severe cracking/pulverization-induced poor cycling stability and unsatisfactory rate capability. Though the strategies such as constructing buffer structures [13] and protection layer coating

[14–16] have been adopted to tackle these key issues, it is still difficult to meet the demand towards high-rate and long-life LIBs.

Polyanionic materials, particularly oxyphosphates, have received much attention as LIB anode materials because of their high structural stability. Oxyphosphates ($MOPO_4$, M = V [17,18], Nb [19], Ti [20,21]) possess the open two-dimensional (2D) or three-dimensional (3D) structures and are suitable for the lithium storage. Moreover, oxygen loss from the framework does not occur due to the robust phosphorous-oxygen covalent bond, thus the phosphate electrodes can provide a stable framework for ion intercalation/deintercalation with a small volume change during the electrochemical process [18,22,23]. Recently, a few reports have demonstrated that the $VOPO_4$-based electrode materials display great application potentials, such as in pseudocapacitors [24] and lithium/sodium ion batteries [17,18,22,25–27]. For example, Xie et al. reported the $VOPO_4$/graphene hybrid film which was used in flexible pseudocapacitors with high energy density [24]. Research on the modified $VOPO_4$ ultrathin nanosheets as cathode materials toward alkali earth ion battery was also reported, which exhibited high rate capability and stable cycling [28]. In this

regards, the exploration of other oxyphosphates for energy storage is necessary and the electrochemical mechanism requires in-depth investigation to understand the structure-performance relationship and hence guide the further material design. Recently, amorphous materials showed potential advantages over crystalline one, including improved tolerance to intrinsic strain and superior charge transfer kinetics [29–31]. Hence, the amorphization of NbOPO$_4$-based materials are expected to exhibit high-rate and stable performances in lithium storage and its Li-storage mechanism has not yet been reported to the best of our knowledge.

Herein, we present an oxyphosphate material NbOPO$_4$ nanosheets as a promising anode material for LIBs. To avoid agglomeration of nanosheets and endow improved lithium storage performances, the composite based on NbOPO$_4$ nanosheets in-situ grown on the reduced graphene oxide is synthesized (denoted as NbOPO$_4$/rGO). Due to the 2D structure together with promoted electron and ion transports, the NbOPO$_4$/rGO composite achieves a high capacity of 502.5 mAh g^{-1} after 800 cycles and reliable rate capability of 308.4 mAh g^{-1} at 8 A g^{-1}. The electrochemical process is in-depth explored via electrochemical analyses and in/ex situ characterizations, which indicates that the lithiation-induced amorphous NbPO$_4$ contributes to the reversible capacity and the generated Li$_3$PO$_4$ behaves as a good lithium ion conductor to endow fast ion transport. The in-depth study of the lithium storage mechanism strengthens the understanding of polyanionic electrode materials and hence will stimulate the further exploration and design of high-performance LIB anode materials.

2. Experimental

2.1. Sample preparation

Synthesis of NbOPO$_4$ nanosheets. 1.2 g of niobium chloride (NbCl$_5$) and 6.65 mL of 85 wt% H$_3$PO$_4$ were added into 28.85 mL of deionized water with stirring for 10 min. Then the mixed solution was transferred to 50 mL Teflon-lined stainless steel autoclave and maintained at 110 °C for 16 h. After cooling down, the white precipitate was washed with the deionized water and acetone. The final product was dried in vacuum at 60 °C for 3 h. Finally, the white powder (denoted as NbOPO$_4$·xH$_2$O) was calcined at 800 °C in Ar for 2 h to obtain the NbOPO$_4$ nanosheets.

Synthesis of NbOPO$_4$/rGO composite. 0.1 g of NbCl$_5$, 1.0 mL of 85 wt% H$_3$PO$_4$ and 1.5 mL of graphene oxide (GO) aqueous dispersion (5 mg mL^{-1}) were added into 30 mL alcohol with stirring for 10 min. Then the mixed solution was transferred to 50 mL Teflon-lined stain autoclave and maintained at 110 °C for 16 h. After cooling down, the precipitate was washed with the deionized water. Finally, the product was freeze-dried to obtain NbOPO$_4$·xH$_2$O/GO. The NbOPO$_4$·xH$_2$O/GO composite was calcined at 800 °C in Ar for 2 h to obtain the NbOPO$_4$ and reduced GO (NbOPO$_4$/rGO) composite.

2.2. Characterization

The X-ray diffraction (XRD) patterns of samples were obtained by D8 Advance X-ray diffractometer with Cu $K\alpha$ radiation. Morphology information was characterized by field-emission scanning electron microscopic (FESEM) using JEOL-7100F microscope. Transmission electron microscopy (TEM) images, high-resolution transmission electron microscopy (HRTEM) images, high angle annular dark field scanning TEM (HAADF-STEM) images, selected area electron diffraction (SAED) pattern and energy dispersive X-ray spectroscopy (EDS) mapping were collected with JEM-2100F STEM/EDS microscope. Raman spectra and atomic force microscopy (AFM) images were obtained by Renishaw INVIN micro-

scopy. The X-ray photoelectron spectroscopy (XPS) data were obtained via Escalab 250Xi instrument. Thermogravimetric-differential scanning calorimetry (TG-DSC) analysis was recorded with Netzsch STA 449F3 simultaneous thermal analyzer. I-V curves were performed by Cryogenics probe station.

2.3. Electrochemical measurements

The electrochemical properties were measured via assembling 2016 coin half-cells with Li metal foil as an anode in a glove box filled with argon. The cathode was prepared by mixing 70 wt% active material, 20 wt% acetylene black and 10 wt% carboxymethyl cellulose (CMC) binder. Then the homogeneous slurry was casted onto Cu foil and dried in oven at 70 °C for 12 h. The mass loading of active material was ~1.5 mg cm^{-2}. The electrolyte was made by dissolving 1.0 M LiPF$_6$ in ethylene carbonate (EC), diethyl carbonate (DC) and dimethyl carbonate (DMC) with the volume ratio of 1:1:1. After being placed under an ambient condition for 12 h, the galvanostatic discharge/charge measurements were carried out in the voltage range of 0.01–3.0 V vs. Li$^+$/Li using LAND battery testing system (CT2001A). The cyclic voltammogram (CV) and electrochemical impedance spectra (EIS) were measured with Autolab PGSTAT 302 electrochemical workstation.

2.4. Theoretical calculations

First-principle calculation based on density functional theory (DFT) was carried out by the CASTEP module implemented in Materials studio software. A generalized gradient approximation (GGA) with the Perdew−Burke−Ernzerhof (PBE) function was employed to describe exchange-correlation interactions. The plane wave cutoff energy was set to be 571.4 eV with the energy precision of 10^{-5} eV. The Brillouin zone (BZ) was sampled by using a 4 × 4 × 6 Gamma-centered Monkhorst-Pack grid. Before calculation of band structure, the geometry of NbOPO$_4$ was fully optimized, including cell parameters and atomic coordinates, until the self-consistent field (SCF) tolerance was less than 10^{-5} eV/Å and the residual forces were less than 0.03 eV/Å. The charge density difference was calculated by subtracting the components' charge densities from their stable composite's charge density. The charge densities were computed using static computations that operated by Vienna Ab-Initio Simulation Package (VASP) with PBE method and the same calculation parameters in CASTEP. The isosurface level was set to be 7.5 × 10^{-5} e/Bohr^3.

3. Results and discussion

As shown in Fig. S1(a), the NbOPO$_4$ framework with the 3D network structure consists of the layers that the NbO$_6$ octahedra are linked together via sharing the oxygen atoms, and further interconnected by the oxygen atoms of PO$_4$ tetrahedra [22]. Due to the layered framework of NbOPO$_4$, the extraneous ions can be stored in the space between the layers. However, the wide band gap implies the poor electron conductivity of NbOPO$_4$ (Fig. S1b). Through constructing the composite NbOPO$_4$/rGO where the NbOPO$_4$ nanosheets in-situ grow on the rGO sheets, the close interaction between NbOPO$_4$ and rGO is expected to alleviate this problem by improving the electronic conductivity. Meanwhile, the well-designed 2D structure of NbOPO$_4$/rGO can provide fast electron/ion transport and avoid aggregation of NbOPO$_4$ nanosheets, resulting in high-rate and stable Li-storage.

As illustrated in Fig. 1(a), the fabrication procedure of the NbOPO$_4$/rGO composite includes two steps. Firstly, the NbOPO$_4$-·xH$_2$O nanosheets were in-situ grown on the graphene oxide sheets
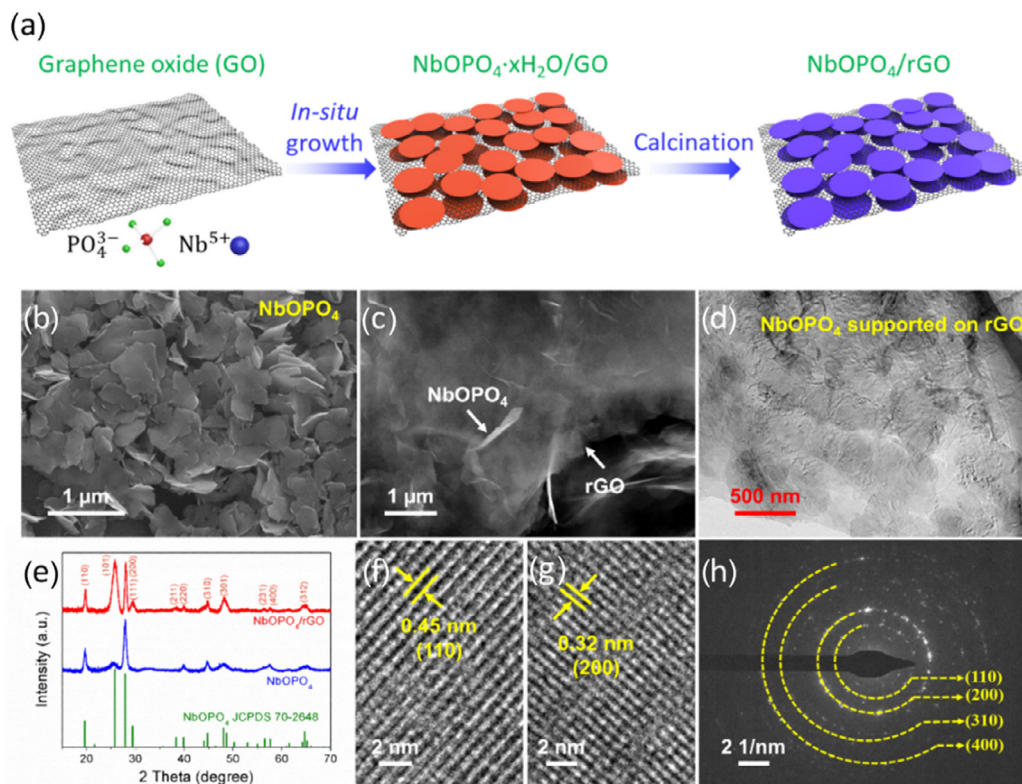
Fig. 1. (a) Schematic illustration of the fabrication procedure for NbOPO$_4$/rGO. (b,c) SEM images of NbOPO$_4$ nanosheets and NbOPO$_4$/rGO, respectively. (d) TEM image of NbOPO$_4$/rGO. (e) XRD patterns of NbOPO$_4$ and NbOPO$_4$/rGO. (f-h) HRTEM images and SAED pattern of NbOPO$_4$/rGO nanosheets.

(NbOPO$_4$·xH$_2$O/GO, as the precursor) by a facile hydrothermal method in the presence of niobium ions (Nb^{5+}), phosphate anions (PO$_4^{3-}$) and GO (Fig. S2a). According to Fig. S2(b), the NbOPO$_4$·xH$_2$O nanosheets are evenly spread over the GO sheets via the *in-situ* growth and they are supposed to tightly connect with each other via oxygen bridges between Nb atoms and oxygen-containing functional groups in GO sheets [32]. For comparison, the GO-free NbOPO$_4$·xH$_2$O nanosheets were also obtained without adding GO sheets during the synthesis process. The NbOPO$_4$·xH$_2$O nanosheets present the thin nanosheet-like morphology with a little aggregation, and the size is ~1 μm (Fig. S2c and S2d). The XRD patterns of NbOPO$_4$·xH$_2$O calcined at different temperatures in the air demonstrate the existence of water molecules (Fig. S2e). The content of water was obtained by TG-DSC result (Fig. S2f). Then the precursors were under heat treatment at 800 °C in Ar atmosphere to obtain the NbOPO$_4$ nanosheets and NbOPO$_4$/rGO composite. As shown in Fig. 1(b), without the rGO support, the obtained NbOPO$_4$ nanosheets show severe stacking due to high surface energy of nanomaterial under high temperture. However, the NbOPO$_4$/rGO composite remains the thin nanosheet-like morphology which is similar to that before calcination (Fig. 1c and Fig. S3). TEM image further demonstrates that the NbOPO$_4$ nanosheets are spread over the supporting rGO sheets (Fig. 1d). The sheet thickness was preliminarily estimated by AFM measurements (Fig. S4). The representative AFM image of the NbOPO$_4$ nanosheet together with the height profile indicates the thickness of ~55 nm in the studied area. While the thickness of the NbOPO$_4$/rGO composite sheet is only ~32 nm, indicating that the rGO substrate can facilitate the distribution of NbOPO$_4$ nanosheets and prevent their aggregation. In addition, such a unique 2D structure ensures high electron conductivity. The electron conductivity of NbOPO$_4$/rGO composite and NbOPO$_4$ were measured using a standard four-probe method on pressed pellets. As shown in Fig. S5, the rGO can greatly enhance the electron conductivity of the whole composite material. The crystalline phase of NbOPO$_4$ nanosheets and NbOPO$_4$/rGO composite was examined by XRD. As presented in Fig. 1(e), the XRD patterns of the calcined samples are well-indexed to the tetragonal NbOPO$_4$ phase (JCPDS NO. 70-2648). And the representative HRTEM images of NbOPO$_4$/rGO reveal the recognizable lattice fringes with interlayer spacing of 0.45 and 0.32 nm, consistent with the (110) and (200) planes for NbOPO$_4$, respectively (Fig. 1f and g). The SAED pattern for NbOPO$_4$/rGO demonstrates a polycrystalline nature (Fig. 1h) with the diffraction rings well-matched with the XRD patterns.

The obtained samples are further identified by the Raman spectra (Fig. 2a). The peaks located at 1348 and 1593 cm^{-1} are attributed to D band and G band of rGO for NbOPO$_4$/rGO, respectively [33,34]. The peak located at 938 cm^{-1} is corresponding to the symmetric stretching vibration of O—P—O bond, and the peak located at 800 cm^{-1} can be attributed to the stretching mode of Nb=O bond [35]. Meanwhile, the peaks below 460 cm^{-1} are assigned to the bending vibration of O—P—O and O—Nb—O bonds [36]. The carbon content in NbOPO$_4$/rGO was determined by CHNS analyses, which indicates the content of rGO in the NbOPO$_4$/rGO composite is estimated to be 3.07 wt% (Fig. S6). TG analysis (Fig. S7) reflects the mass loss of 3.81% in air, similar to the carbon content obtained by CHNS analyses, which is attributed to the removal of adsorbed water and rGO. The even distribution of NbOPO$_4$ nanosheets on the supporting rGO sheets is confirmed by HAADF-STEM and elemental mappings (Fig. 2b). As seen, the Nb, P, O, and C elements are distributed evenly on the whole sheets. It is noted that the obvious Moiré fringes demonstrate that NbOPO$_4$ nanosheets do not aggregate together but are stacked at the Van der Waals distance (Fig. 2c and Fig. S8) [37]. This feature promotes the horizontal ion transport for the more efficient energy storage. Meanwhile, only a small number of Moiré fringes are observed in NbOPO$_4$ nanosheets
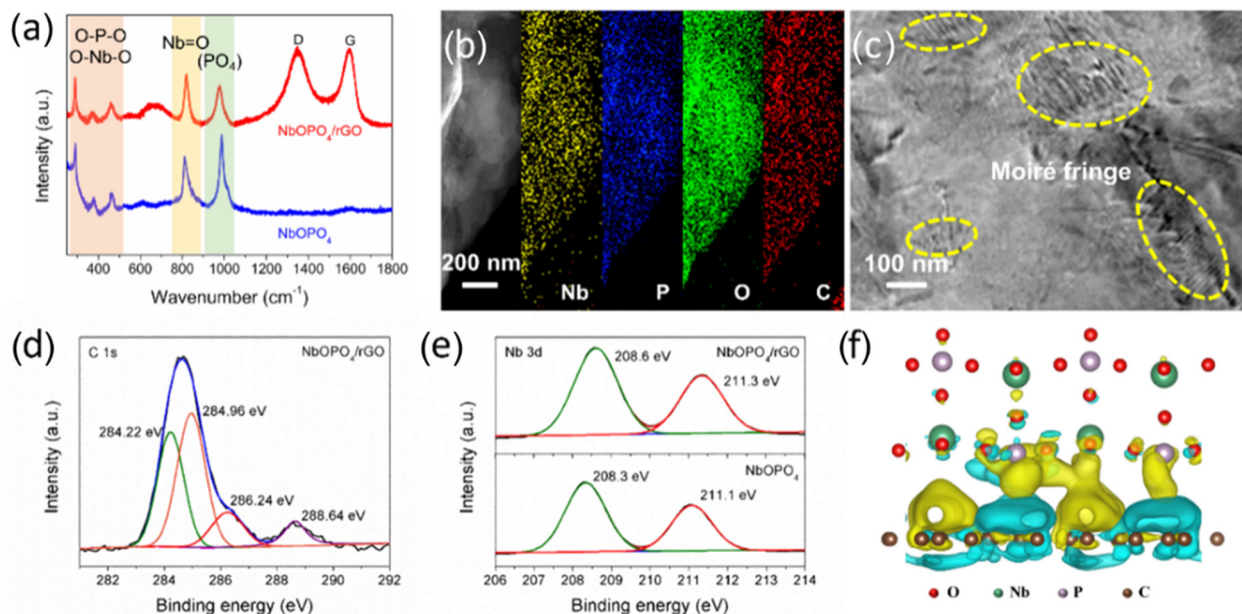
Fig. 2. (a) Raman spectra of $NbOPO_4$ and $NbOPO_4$/rGO. (b,c) HAADF-STEM image and elemental mapping and TEM image of $NbOPO_4$/rGO. (d) High-resolution C 1s XPS spectra of $NbOPO_4$/rGO. (e) High-resolution Nb 3d XPS spectra of $NbOPO_4$/rGO and $NbOPO_4$. (f) 3D contour plot of charge density difference of $NbOPO_4$/rGO. The yellow and blue regions represent charge accumulation and depletion, respectively.

compared with $NbOPO_4$/rGO, indicating severe aggregation of nanosheets without the rGO support (Fig. S9). In addition, the valence state of the $NbOPO_4$ nanosheets and $NbOPO_4$/rGO composite was investigated by XPS. The C 1s spectra of $NbOPO_4$/rGO (Fig. 2d) are well fitted by four peaks at 284.2, 285.0, 286.2, and 288.6 eV, consistent with C—C, C=C, C—O—C, O—C=O, respectively [38,39]. The XPS peaks of 208.3 and 211.1 eV in high-resolution Nb 3d spectra of $NbOPO_4$ (Fig. 2e) can be ascribed to Nb $3d_{5/2}$ and Nb $3d_{3/2}$, respectively [40]. The obvious increase of binding energy for $NbOPO_4$/rGO indicates the enhanced electronegativity of Nb in $NbOPO_4$/rGO compared to that in $NbOPO_4$. This can be attributed to the residual oxygen in rGO, which strengthens the chemical interaction between $NbOPO_4$ and rGO to promote the electron conductivity. This phenomenon has also been reported in the MoS_2/rGO composite where the increased binding energy of Mo 3d in MoS_2/rGO when compared with that in MoS_2 was attributed to the interaction of Mo in MoS_2/rGO with the residual oxygen of rGO [41]. Furthermore, a charge concentration enhanced area exists in the $NbOPO_4$-rGO interface which is reflected by the difference in charge density for $NbOPO_4$ and rGO (Fig. 2f) and hence further indicates the interaction between $NbOPO_4$ and rGO. Such interaction can effectively strengthen the affiliation between $NbOPO_4$ and rGO and promote the electron transport [42].

The electrochemical performances of the $NbOPO_4$/rGO composite as the anode for LIBs were assessed. Firstly, the CV was carried out at a scan rate of 0.1 mV s^{-1} in the voltage range of 0.01–3.0 V (Fig. 3a). In the first cycle, the reduction peaks at 1.35 and 1.10 V can be ascribed to the reduction of Nb^{5+} during the Li$^+$-insertion into $NbOPO_4$/rGO and the peak at 0.85 V is assigned to the formation of solid electrolyte membrane (SEI) layer on the surface of the electrode material. The overlap of the second and the third cycle CV curves implies the excellent reversibility of the electrochemical reaction during cycling. The similar CV curves of the rGO-free $NbOPO_4$ nanosheets indicate that the presence of rGO does not change the electrochemical reaction mechanism (Fig. S10) but regulate the lithium storage performances of $NbOPO_4$ [43], which will be demonstrated in detail below. The discharge profiles of $NbOPO_4$/rGO at 500 mA g^{-1} in the first three cycles shows two irre-

versible platforms at about 1.35 V and 1.10 V (Fig. S11), in consistence with the result of CV curves. The loss of capacity is mainly caused by the formation of SEI film on the electrode surface in the first cycle. After that, the electrochemical reaction shows high reversibility. The rate performance was studied to evaluate the potential application of this material in the high-power devices. As shown in Fig. 3(b and c), the much better rate performance is achieved on $NbOPO_4$/rGO than the $NbOPO_4$ nanosheets. In detail, the $NbOPO_4$/rGO delivers an average discharge capacity of 582.8, 545.3, 500.0, 452.6, 416.6, 353.2, and 308.4 mAh g^{-1} at 100, 200, 500, 1000, 2000, 5000, and 8000 mA g^{-1}, respectively. And when the applied current density comes back to 100 mA g^{-1}, the stable capacity of 480 mAh g^{-1} can be obtained. To further figure out the excellent electrochemical performance of $NbOPO_4$/rGO, the EIS tests of $NbOPO_4$/rGO and $NbOPO_4$ were measured (Fig. 3d). From the Nyquist plots, the semicircle from high-medium frequencies and the sloping line represent the charge-transfer resistance (R_{ct}) at the interface between electrolyte and electrode and the diffusion resistance of lithium ions inside the electrode materials (R_w), respectively [42,44]. The much smaller diameter of the semicircle for $NbOPO_4$/rGO demonstrates its greatly enhanced charge transfer dynamics and electronic conductivity. Moreover, the larger slope angle of $NbOPO_4$/rGO at low frequencies indicates the improved lithium ion diffusion kinetics inside the electrode material [45].

Furthermore, the improved cycling stability of $NbOPO_4$/rGO over the rGO-free $NbOPO_4$ was obtained (Fig. 3e). After being activated at current density of 100 mA g^{-1} for 5 cycles and then measured at 500 mA g^{-1}, the discharge capacity of 502.5 mAh g^{-1} after 800 cycles is obtained for $NbOPO_4$/rGO, with a capacity retention of 85.4%, which is over two-fold higher than that of simplex $NbOPO_4$ nanosheets. It is worth noting that the original discharge capacity of rGO is 280.1 mAh g^{-1}. If calculating the contribution of rGO based on the content of rGO, it only contributes to 8.6 mAh g^{-1} for the whole capacity of $NbOPO_4$/rGO (Fig. S12). The big capacity difference between $NbOPO_4$/rGO and $NbOPO_4$ is due to the regulating role of rGO which accelerates the electrochemical reaction of active materials. In addition, we also investigated the cycling
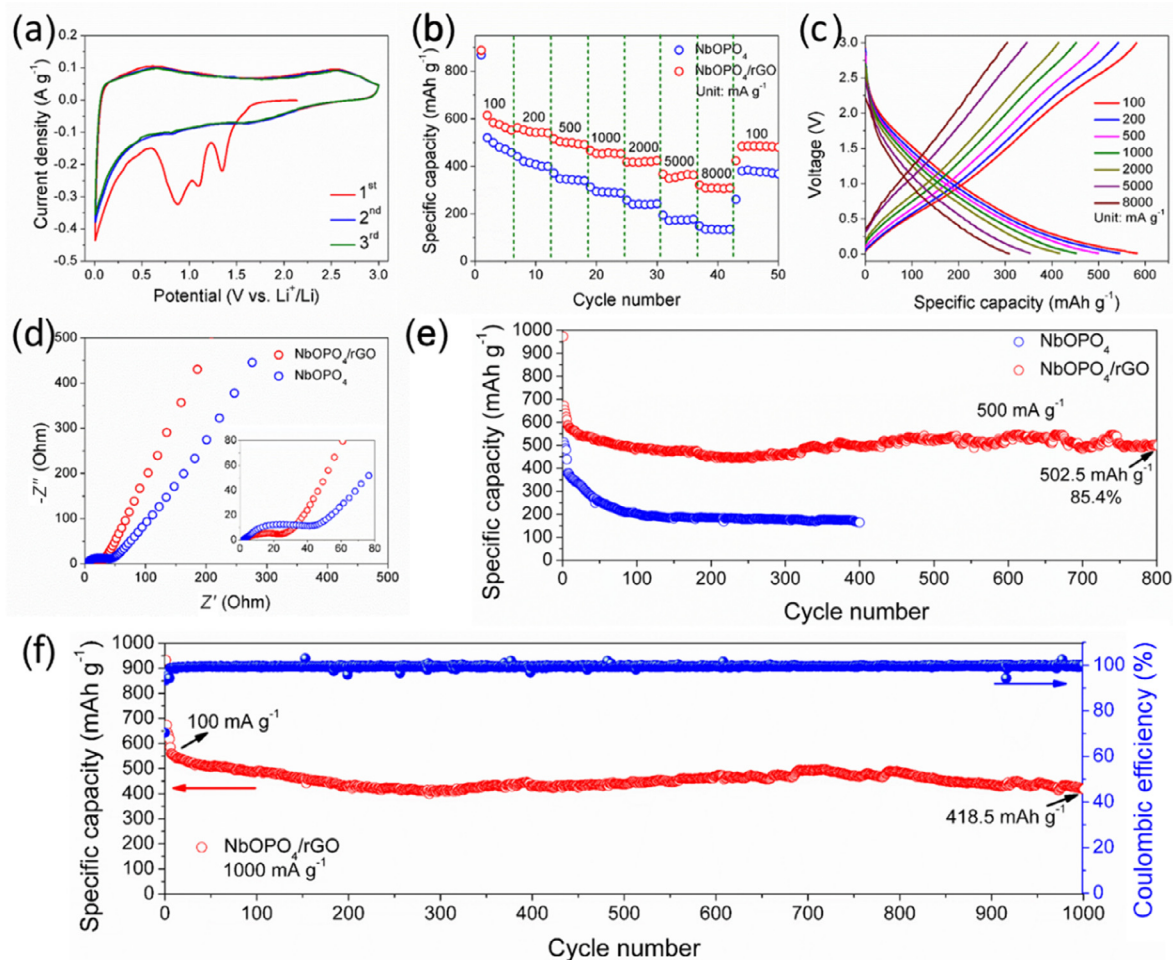
Fig. 3. Electrochemical performances of NbOPO$_4$ and NbOPO$_4$/rGO anodes at 0.01–3.0 V. (a) CV curves of NbOPO$_4$/rGO at 0.1 mV s^{-1}. (b) Rate performances of NbOPO$_4$ and NbOPO$_4$/rGO at different current densities of 100, 200, 500, 1000, 2000, 5000, and 8000 mA g^{-1}, respectively. (c) Discharge/charge profiles of NbOPO$_4$/rGO at different current densities. (d) Nyquist plots in a frequency ranging from 100 kHz to 0.1 Hz for NbOPO$_4$ and NbOPO$_4$/rGO. (e) Long cycling performance of NbOPO$_4$/rGO and NbOPO$_4$ measured at 500 mA g^{-1} after being activated at 100 mA g^{-1} for 5 cycles. (f) Long cycling performance of NbOPO$_4$/rGO measured at 1000 mA g^{-1} after being activated at 100 mA g^{-1} for 5 cycles.

performance at a larger current density of 1000 mA g^{-1} for NbOPO$_4$/rGO after being activated at 100 mA g^{-1} for 5 cycles (Fig. 3f). The discharge capacity sharply decreases in the first few cycles and then remains at a steady discharge capacity to 418.5 mAh g^{-1} after 1000 cycles. The NbOPO$_4$/rGO electrode displays the coulombic efficiency (CE) of about 100% during cycling following the initial cycle. The initial CE is 70.4%, which is mainly ascribed to the decomposition of organic electrolyte and the generation of SEI layer as well as some irreversible reactions. TEM images of NbOPO$_4$/rGO and NbOPO$_4$ after cycling at 500 mA g^{-1} (Fig. S13) indicates that the morphology of nanosheets for NbOPO$_4$/rGO remains unchanged. In contrast, the morphology for rGO-free NbOPO$_4$ is greatly damaged after cycling. The existence of rGO sheets can effectively avoid the nanosheet agglomeration during cycling, thus maintaining the integrity of nanosheets. In addition, compared with the previously reported single/mixed metal oxides-based anode materials and other reported phosphate materials, the as-synthesized NbOPO$_4$/rGO exhibits superior cycling stability and high rate capability (Tables S1 and S2). Particularly, a high capacity ratio of 52.9%-8000/100 (8000 and 100 correspond to the tested highest and lowest current density, respectively, and 52.9% represents the calculated ratio of the discharge capacity at 8000 mA g^{-1} to that at 100 mA g^{-1}) is achieved for NbOPO$_4$/rGO, higher than those in most previous reports, such as CoO@BNG

(17.0%-3000/100) [42], iron oxide/rGO (~35%-7000/500) [46], and SnO$_2$-based (27.6%-5000/100) [47].

To reveal the electrochemical process, CV curves at the scan rates of 0.2 to 1.0 mV s^{-1} were carried out for NbOPO$_4$/rGO and NbOPO$_4$ as shown in Fig. 4(a and b). The percent of capacitive contribution increases with the increase of scan rate for both NbOPO$_4$/rGO and NbOPO$_4$ (Fig. 4c) [48]. Due to the short ion diffusion distance and fast electron transport for NbOPO$_4$/rGO nanosheets, its diffusion contribution is higher than that for NbOPO$_4$. It should be noted that the reduction peaks at 1.35 ad 1.10 V only exist in the first CV during the electrochemical measurement at 0.01–3.0 V and disappear in the following cycles. A series of CV tests were then carried out in the different voltage ranges to uncover its Li storage mechanism (Fig. 4d and S14). As can be seen, when tested at 1.1–3.0 V and 1.3–3.0 V, a couple of oxidation/reduction peaks (1.55/1.95 V) can be observed. However, the oxidation peak at 1.95 V disappears when carried out at 0.9–3.0 V and 0.01–3.0 V, indicating the lithiation reaction at 1.55 V is reversible but that at 1.08 V is irreversible. As mentioned above, the oxidation peak at 0.85 V is mainly attributed to the generation of SEI layer. The electrochemical mechanism was further revealed by *in-situ* XRD measurement (Fig. 4e). Firstly, the peak of (200) at 27.9° for NbOPO$_4$ slightly shifts to the lower 2θ positions during discharging, indicating a solid solution insertion process without changing the main
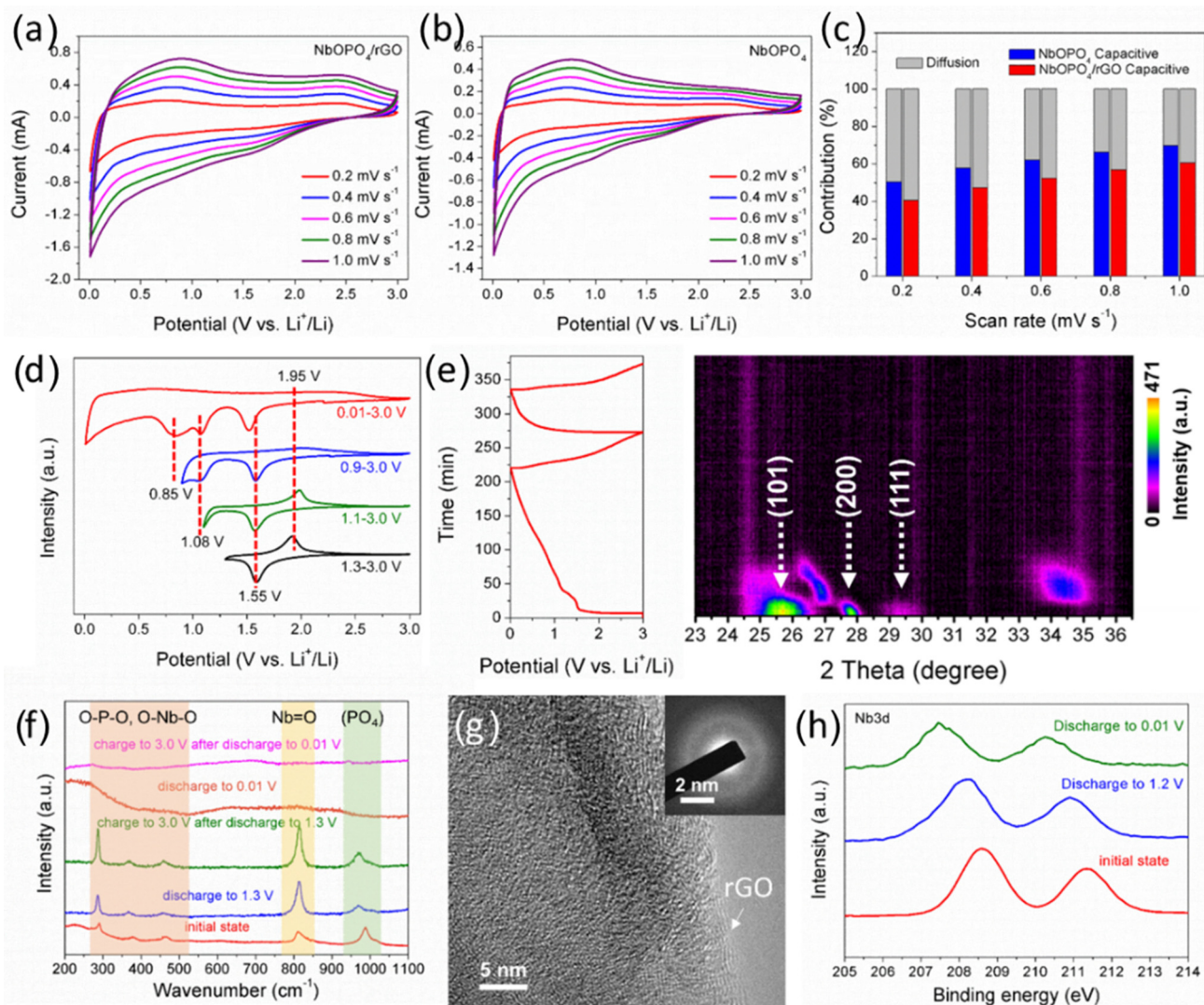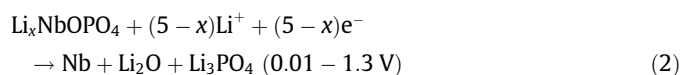
Fig. 4. (a,b) Cyclic voltammetry of NbOPO$_4$/rGO and NbOPO$_4$ in the second cycle. (c) Normalized contribution ratio of capacitive (red and blue) and diffusion-controlled (gray) capacities at various scan rates. (d) CV curves of NbOPO$_4$/rGO in different voltage ranges. (e) *In-situ* XRD results of NbOPO$_4$/rGO during the galvanostatic discharge/charge processes. (f) *Ex-situ* Raman spectra of NbOPO$_4$/rGO. (g) HRTEM image of NbOPO$_4$/rGO when discharging to 0.01 V, and the inset in (g) is the corresponding SAED pattern. (h) High-resolution Nb 3*d* XPS spectra of NbOPO$_4$/rGO at different states.

crystal structure. Then after discharging to below 1.3 V, the new peaks located at 26.9° and 34.5° emerge, which suggests the formation of new lithiated product. The formation of new phase is speculated to intermediate phase for the conversion reaction during the following lithiation process. After full discharging, the peaks of (101), (200) and (111) for NbOPO$_4$ disappear, which indicates that the amorphization of electrode. Besides, these peaks do not re-appear during the subsequent charging process, which suggests that the electrode material occurs in an amorphous state in the subsequent electrochemical reaction and further implies that the NbOPO$_4$ is a conversion-type anode material for LIBs [49,50].

Ex-situ Raman/XPS/XRD were also carried out to probe the reaction mechanism at each stage. When discharging to 1.3 V and then charging to 3.0 V, the Raman spectra are as same as the initial state, which reveals the unchanged crystal structure and the reversible reaction (Fig. 4f). When discharging to 0.01 V and then charging to 3.0 V, these Raman peaks disappear. The *ex-situ* XRD results (Fig. S15) confirm the formation of amorphous phase, and the HRTEM image for NbOPO$_4$ after discharging to 0.01 V further demonstrates the amorphous characteristic of the discharged pro-

duct (Fig. 4g). In addition, the *ex-situ* XPS was measured to explore the chemical state change of element Nb for NbOPO$_4$/rGO during discharging (Fig. 4h). Both Nb 3$d_{3/2}$ and Nb 3$d_{5/2}$ peaks shift to the lower binding energy during discharging, suggesting the reduction of Nb^{5+}. When discharging to 0.01 V, the Nb 3$d_{3/2}$ and Nb 3$d_{5/2}$ peaks located at 210.28 and 207.51 eV can be attributed to NbO$_x$/ Nb according to previous reports [51,52]. The existence of the oxidative NbO$_x$ species may originate from the oxidation of the nanoscaled niobium metal in the air. From the above-mentioned results and referring to the electrochemical mechanism of analogous VOPO$_4$ anode, the electrochemical process of NbOPO$_4$ as the LIB anode is speculated as follows.

$$NbOPO_4 + xLi^+ + xe^- \leftrightarrow Li_xNbOPO_4 \ (1.3 - 3.0 \ V) \tag{1}$$

$$Li_xNbOPO_4 + (5 - x)Li^+ + (5 - x)e^-$$
$$\rightarrow Nb + Li_2O + Li_3PO_4 \ (0.01 - 1.3 \ V) \tag{2}$$

$$NbPO_4 + 3Li^+ \leftrightarrow Nb + Li_3PO_4 \ (0.01 - 3.0 \ V) \tag{3}$$

In the initial discharging stage, the intercalation reaction happens at ~1.55 V to form Li_xNbOPO_4 in equation (1). Then while discharging to 0.01 V, the irreversible conversion reaction shown in Eq. (2) results in the formation of Nb, Li_2O and Li_3PO_4. At such stage, the generation of SEI layer inevitably causes the loss of capacity. In the subsequent charge/discharge processes, the reversible reaction in (3) plays a vital role in providing the main capacity of electrode, which is similar to the case in $VOPO_4$ anode [18]. It is noted that the product Li_3PO_4 can behave with a high lithium ion mobility to promote ion transmission compared with Li_2O, which greatly accelerates reaction kinetics [53,54].

The $NbOPO_4$/rGO composite delivers high rate capability and outstanding cycling stability in lithium storage. The superior electrochemical performances compared to $NbOPO_4$ can be assigned to the following reasons. The 2D structure of rGO supported $NbOPO_4$ increases contact area between active material and electrolyte to provide high activity of $NbOPO_4$, and the product Li_3PO_4 as ionic conductor promotes lithium ion mobility. Moreover, rGO sheets not only avoid the self-stacking of nanosheets, but also act as electron diffusion channels to accelerate electron transport at the rGO/active material interface. These can be well demonstrated via the mechanism model proposed by Zheng et al. [55,56]. Fast ion/electron transport eventually results in high-rate performance. Besides, the robust 2D structure of composite relieves the volume expansion during the charge/discharge processes and remains the structural integrity, which guarantees the cycling stability.

4. Conclusions

In summary, we have investigated the electrochemical process of $NbOPO_4$ as a new anode material for LIBs. Further analyses on the lithium storage mechanism for the rGO-supported $NbOPO_4$ nanosheets as a two-dimensional anode material were carried out via the in/ex situ XRD and *ex-situ* Raman/XPS. The results indicate that following the initial intercalation-conversion reaction, the reversible conversion between the lithiation-induced amorphous $NbPO_4$ and Nb occurs, which contributes to the high reversibility and rate capability during the subsequent cycling. Compared to $NbOPO_4$, the $NbOPO_4$/rGO composite material also exhibits greatly enhanced electrochemical performances, particularly reversible capacity, due to the regulating roles of rGO including avoiding the self-aggregation of $NbOPO_4$ nanosheets and facilitating electron/ion transports. Meanwhile benefiting from the ionic-conductor feature of Li_3PO_4 generated during cycling, the composite achieves a discharge capacity of 502.5 mAh g^{-1} at 500 mA g^{-1} after 800 cycles, with a high capacity retention of 85.4%. Even when tested at 8000 mA g^{-1}, a reliable discharge capacity of 308.4 mAh g^{-1} is acquired. Our study reveals the electrochemical process of phosphate based polyanionic materials, which will stimulate the development of these materials in achieving high-performance rechargeable metal-ion batteries.

Declaration of Competing Interest

The authors declare that they have no known competing financial interests or personal relationships that could have appeared to influence the work reported in this paper.

Acknowledgments

Appendix A. Supplementary data

Supplementary data to this article can be found online at https://doi.org/10.1016/j.jechem.2020.05.004.

References

[1] M. Armand, J.M. Tarascon, Nature 451 (2008) 652–657.
[2] M. Li, J. Lu, Z. Chen, K. Amine, Adv. Mater. 30 (2018) 1800561.
[3] L. Mai, M. Yan, Y. Zhao, Nature 546 (2017) 469–470.
[4] D. Bruce, K. Haresh, T. Jean-Marie, Science 334 (2011) 928–935.
[5] P. Bhattacharya, D. Suh, P. Nakhanivej, Y. Kang, H. Park, Adv. Funct. Mater. 28 (2018) 1801746.
[6] J. Dong, Y. Xue, C. Zhang, Q. Weng, P. Dai, Y. Yang, M. Zhou, C. Li, Q. Cui, X. Kang, C. Tang, Y. Bando, D. Golberg, X. Wang, Adv. Mater. 29 (2017) 1603692.
[7] J. Lu, Z. Chen, F. Pan, Y. Cui, K. Amine, Electrochem. Energy Rev. 1 (2018) 35–53.
[8] Y. Deng, C. Fang, G. Chen, J. Power Sources 304 (2016) 81–101.
[9] L. Sheng, S. Liang, T. Wei, J. Chang, Z. Jiang, L. Zhang, Q. Zhou, J. Zhou, L. Jiang, Z. Fan, Energy Storage Mater. 12 (2018) 94–102.
[10] Q. Xu, J. Sun, Z. Yu, Y. Yin, S. Xin, S. Yu, Y. Guo, Adv. Mater. 30 (2018) 1707430.
[11] X. Cao, Y. Fan, J. Qu, T. Wang, D. Legut, Q. Zhang, J. Energy Chem. 47 (2020) 160–165.
[12] J. Liu, J. Liang, C. Wang, J. Ma, J. Energy Chem. 33 (2019) 160–166.
[13] T. Ma, X. Liu, L. Sun, Y. Xu, L. Zheng, J. Zhang, J. Energy Chem. 34 (2019) 43–51.
[14] J. Meng, X. Liu, J. Li, Q. Li, C. Zhao, L. Xu, X. Wang, F. Liu, W. Yang, X. Xu, Z. Liu, C. Niu, L. Mai, Nano Lett. 17 (2017) 7773–7781.
[15] B. Guan, L. Yu, J. Li, X. Lou, Sci. Adv. 2 (2016) 1501554.
[16] Y. Liu, P. Zhang, N. Sun, B. Anasori, Q. Zhu, H. Liu, Y. Gogotsi, B. Xu, Adv. Mater. 30 (2018) 1707334.
[17] Y. Zhu, L. Peng, D. Chen, G. Yu, Nano Lett. 16 (2015) 742–747.
[18] B. Zhang, Y. Han, J. Zheng, J. Zhang, C. Shen, L. Ming, X. Yuan, H. Li, Chem. Commun. 50 (2014) 11132–11134.
[19] S. Patoux, C. Masquelier, Chem. Mater. 14 (2002) 2334–2341.
[20] P. Bleith, M. Valla, P. Novák, C. Villevieille, J. Mater. Chem. A 2 (2014) 12513–12518.
[21] I. Belharouak, K. Amine, Electrochem. Commun. 7 (2005) 648–651.
[22] Y. Sun, C. Wu, Y. Xie, J. Nanopart. Res. 12 (2009) 417–427.
[23] K. Lasri, I. Saadoune, K. Edström, Procedia Eng. 138 (2016) 281–290.
[24] C. Wu, X. Lu, L. Peng, K. Xu, X. Peng, J. Huang, G. Yu, Y. Xie, Nat. Commun. 4 (2013) 3431–3437.
[25] H. Li, L. Peng, Y. Zhu, D. Chen, X. Zhang, G. Yu, Energy Environ. Sci. 9 (2016) 3399–3405.
[26] G. He, W. Kan, A. Manthiram, Chem. Mater. 28 (2016) 682–688.
[27] L. Peng, Y. Zhu, X. Peng, Z. Fang, W. Chu, Y. Wang, Y. Xie, Y. Li, J. Cha, G. Yu, Nano Lett. 17 (2017) 6273–6279.
[28] L. Zhou, Q. Liu, Z. Zhang, K. Zhang, F. Xiong, S. Tan, Q. An, Y. Kang, Z. Zhou, L. Mai, Adv. Mater. 30 (2018) 1801984.
[29] K. Gyutae, J. Sookyung, S. Ju-Hyeon, C. Jaephil, L. Heon, ASC Nano 8 (2014) 1907–1912.
[30] X. Liu, J. Zhang, W. Si, L. Xi, S. Oswald, C. Yan, O. Schmidt, Nanoscale 7 (2015) 282–288.
[31] L. Lin, X. Xu, C. Chu, M. Majeed, J. Yang, Angew. Chem. Int. Ed. 55 (2016) 14063–14066.
[32] G. Zhou, D. Wang, L. Yin, N. Li, F. Li, H. Cheng, ACS Nano 6 (2012) 3214–3223.
[33] W. Wen, M. Zou, Q. Feng, J. Li, H. Lai, Z. Huang, J. Energy Chem. 25 (2016) 445–449.
[34] M. Zhao, Q. Zhang, J. Huang, G. Tian, J. Nie, H. Peng, F. Wei, Nat. Commun. 5 (2014) 1–8.
[35] G. Stranford, R. Sr, J. Solid State Chem. 76 (1988) 407–411.
[36] L. Moreno-Real, E. Losilla, M. Aranda, M. Martʀ Nez-Lara, S. Bruque, M. Gabás, J. Solid State Chem. 137 (1998) 289–294.
[37] C. Yan, C. Lv, Y. Zhu, G. Chen, J. Sun, G. Yu, Adv. Mater. 29 (2017) 1703909.
[38] Y. Wang, Z. Chen, T. Lei, Y. Ai, Z. Peng, X. Yan, H. Li, J. Zhang, Z. Wang, Y. Chueh, Adv. Energy Mater. 8 (2018) 1703453.
[39] X. Liu, K. Ni, B. Wen, C. Niu, J. Meng, R. Guo, Q. Li, J. Li, Y. Zhu, X. Wu, D. Zhao, L. Mai, J. Mater. Chem. A 6 (2018) 17874–17881.
[40] X. Wang, Q. Li, L. Zhang, Z. Hu, L. Yu, T. Jiang, C. Lu, C. Yan, J. Sun, Z. Liu, Adv. Mater. 30 (2018) 1800963.
[41] Y. Liu, L. Jiao, Q. Wu, Y. Zhao, K. Cao, H. Liu, Y. Wang, H. Yuan, Nanoscale 5 (2013) 9562–9567.
[42] H. Tabassum, R. Zou, A. Mahmood, Z. Liang, Q. Wang, H. Zhang, S. Gao, C. Qu, W. Guo, S. Guo, Adv. Mater. 30 (2018) 1705441.
[43] R. Fang, K. Chen, L. Yin, Z. Sun, F. Li, H. Cheng, Adv. Mater. 31 (2019) 1800863.
[44] Y. Chu, L. Guo, B. Xi, Z. Feng, F. Wu, Y. Lin, J. Liu, D. Sun, J. Feng, Y. Qian, S. Xiong, Adv. Mater. 30 (2018) 1704244.
[45] Z. Cai, L. Xu, M. Yan, C. Han, L. He, K. Hercule, C. Niu, Z. Yuan, W. Xu, L. Qu, Nano Lett. 15 (2014) 738–744.
[46] A. AbdelHamid, Y. Yu, J. Yang, J. Ying, Adv. Mater. 29 (2017) 1701427.
[47] L. Xia, S. Wang, G. Liu, L. Ding, D. Li, H. Wang, S. Qiao, Small 12 (2016) 853–859.

[48] X. Xu, C. Niu, M. Duan, X. Wang, L. Huang, J. Wang, L. Pu, W. Ren, C. Shi, J. Meng, B. Song, L. Mai, Nat. Commun. 8 (2017) 1–11.
[49] J. Wang, G. Zhang, Z. Liu, H. Li, Y. Liu, Z. Wang, X. Li, K. Shih, L. Mai, Nano Energy 44 (2018) 272–278.
[50] N. Chen, Y. Yao, D. Wang, Y. Wei, X. Bie, C. Wang, G. Chen, F. Du, ACS Appl. Mater. Inter. 6 (2014) 10661–10666.
[51] E. Latta, M. Ronay, J. Vac. Sci. Technol. A 4 (1986) 1626–1630.
[52] J. Jouve, Y. Belkacem, C. Severac, Thin Solid Films 139 (1986) 67–75.
[53] N. Kuwata, N. Iwagami, Y. Matsuda, Y. Tanji, J. Kawamura, ECS Trans. 16 (2009) 53–60.
[54] H. Jodi, S. Supardi, E. Kartini, A. Zulfia, Indonesian, J. Mater. Sci. 18 (2016) 1–8.
[55] W. Zhang, D. Wang, W. Zheng, J. Energy Chem. 41 (2020) 100–106.
[56] D. Wang, W. Zhang, N. Drewett, X. Liu, S. Yoo, S. Lee, J. Kim, T. Deng, X. Zhang, X. Shi, W. Zheng, ACS Cent. Sci. 4 (2018) 81–88.